

Contents lists available at ScienceDirect

Wear

journal homepage: www.elsevier.com/locate/wear





Microstructure and tribocorrosion behaviors of Fe–Al–Ti coatings prepared by the aluminothermic reaction

H. Chen*, R.P. Li, S. Guo, Z. Zhang, X.X. Li, X.L. Zhao

School of Materials Science and Engineering, Liaocheng University, Liaocheng, Shandong, 252000, China

ARTICLE INFO

Keywords: Aluminothermic reaction Fe_Al_Ti coatings Tribocorrosion Synergistic effects

ABSTRACT

To improve the tribocorrosion resistance of 316L stainless steel in acidic media, Fe–Al–Ti coatings were prepared on 316L substrate by self-propagating high-temperature synthesis (SHS) using an aluminothermic reaction. The effects of Ti content on the tribocorrosion behaviors of Fe–Al–Ti coatings in 0.5 mol/L $\rm H_2SO_4$ solutions were investigated. The Fe–Al–Ti coatings exhibited a multi-phase microstructure. The open circuit potential (OCP) of the Fe–Al–Ti coatings and 316L substrate decreased significantly with the onset of sliding, indicating a strong wear-corrosion synergistic effect. The hardness and tribocorrosion resistance of Fe–Al–Ti coatings increase with increasing the Ti content. The tribocorrosion volume loss of the Fe–25Al–25Ti coating was about one order of magnitude lower than that of the 316L substrate. The Fe–25Al–25Ti coating was more suitable as a tribocorrosion-resistant material than the 316L substrate.

1. Introduction

Wear and corrosion are the two most common failure modes of contact moving mechanical components operating under corrosive conditions [1,2]. Furthermore, when two failure modes coexist (defined as tribocorrosion), their interaction tends to cause more severe material damage than either wear or corrosion alone [3]. Austenitic stainless steels with high Cr contents are widely used in mild and acid solutions such as chemical, medical, marine, acid pickling, and acid etching industries due to their good corrosion properties and excellent forming characteristics [4–6]. Unfortunately, austenitic stainless steel has low hardness, which results in poor wear resistance under abrasive and adhesive conditions [7]. Therefore, its application as a tribocorrosion-resistant material is severely limited. One of the most effective methods is to utilize surface modification to obtain a protective coating with excellent anti-wear and anti-corrosion properties [8,9].

Fe–Al-based alloys are considered to be an attractive material for industrial applications under extreme conditions due to their low cost, outstanding corrosion resistance, and good wear behavior [10–12]. However, serious room temperature brittleness hinders their industrial application as structural materials. To overcome this issue, the preparation of a high-hardness Fe–Al intermetallic coating on the surface of a softer substrate material (such as stainless steel) has become an effective solution [13]. Recent studies [14,15] have also shown that the alloying

elements play an important role in improving the toughness, corrosion, and wear properties of Fe-Al intermetallic compounds. In Fe-Al-Ti ternary intermetallic alloys, the beneficial effects of Ti on high-temperature strength, creep, and oxidation resistance have been confirmed [16]. Compared to Fe-Al binary alloys, ternary Fe-Al-Ti intermetallic alloys exhibit higher yield strength and creep resistance above 800 °C due to the formation of Fe₂TiAl Heusler alloy with L2₁ crystal structure and high melting point [17,18]. The strength and ductility of Fe-Al-Ti alloys increase with Al and Ti content (ranging from 8.5 to 20 and 21-25 at.%, respectively) due to Laves phase precipitates (formation of L21+C14 structure) or coherent L21+A2 microstructure [19-21]. The Fe₂TiAl Heusler alloy is also expected to have excellent wear resistance due to its high melting point, high hardness, and strong covalent bonds [22]. However, the related investigations are still insufficient, especially the research on the tribocorrosion properties of Fe-Al-Ti alloy is rarely reported.

In recent years, several surface engineering technologies have been reported for preparing intermetallic coatings, including spray coating [23], pack cementation [24], laser cladding [25], electro-depositing [26], and chemical vapor deposition (CVD) [27]. However, these preparation techniques usually require expensive specialized equipment and have the drawbacks of high energy consumption, high preparation costs, and environmental pollution [28]. Self-propagating high-temperature synthesis (SHS) is a novel method for preparing coating

E-mail address: chenhui@lcu.dedu.cn (H. Chen).

^{*} Corresponding author.

materials that combine material synthesis and coating preparation in one step [29]. Compared to other technologies, the SHS coating method offers many advantages, such as simplicity, low cost and energy consumption, and good industrial application prospects. In this study, Fe–Al–Ti coatings were prepared on 316L substrate using Fe, Fe₂O₃, TiO₂ and Al powders as starting materials via the SHS process. The aluminothermic reaction between Fe₂O₃, TiO₂ and Al is highly exothermic, allowing the self-propagating combustion reaction to continue until completion. The effects of Ti content on the microstructure and tribocorrosion behaviors of Fe–Al–Ti coatings in 0.5 mol/L $\rm H_2SO_4$ solutions were investigated, and the tribocorrosion mechanism was elucidated.

2. Experimental procedure

2.1. Coating preparation

The Fe-25Al-5Ti, Fe-25Al-15Ti, and Fe-25Al-25Ti (at. %) coatings were prepared on commercial 316L stainless steel substrate (Φ 25 mm \times 8 mm) using the SHS process. Starting materials included Fe₂O₃ (99.5%), TiO2 (99.9%), Al (99%) and Fe (99.5%) powders with an average particle size ranging from 40 to 150 µm. Prior to SHS processing, 316L substrates were polished up to #800 with SiC paper to eliminate surface impurities and improve adhesion. The average roughness (Ra) of the substrate before and after polishing was $0.2~\mu m$ and 0.087μm, respectively. The substrates were then ultrasonically cleaned with alcohol for 10 min and dried. Raw powders (35 g) were mixed at a speed of 150 rpm for 5 h in a planetary ball mill with Al₂O₃ spheres. The mixed powders were cold-pressed into a cylinder (25 mm in diameter) under a uniaxial pressure of 50 MPa. The cylinder was placed on a 316L substrate and high-purity argon gas was introduced into the furnace chamber at a flow rate of 20 ml/min for protection. Subsequently, the cylinders were heated to 600 °C for 15 min and ignited using a tungsten filament, resulting in an aluminothermic reaction of the reactant according to the following reaction:

$$2Al + Fe_2O_3 = Al_2O_3 + 2Fe$$
 (1)

$$4A1 + 3TiO_2 = 2Al_2O_3 + 3Ti$$
 (2)

$$7Fe + 2Al + 2Ti = Fe2TiAl + Fe3Al + Fe2Ti$$
 (3)

All products were melted due to overheating during the reaction. The Al_2O_3 with a lower density floats on the upper layer of combustion products. The products were then cooled down in the furnace under the protection of argon. Then the products were taken out from the furnace at room temperature, and the Al_2O_3 layer on the 316L substrate can be removed manually. The samples were then cut into 10 mm x 10 mm x 5 mm specimens using Electric Discharge Machining (EDM, DK7740-B, China). The Fe–Al–Ti coated surfaces were mechanically ground and polished using waterproof abrasive sandpaper (from 400 to 1500 grit) and 1 μ m diamond grain paste for corrosion and tribocorrosion testing.

2.2. Tribocorrosion tests

The tribocorrosion tests were conducted using a reciprocating sliding tribometer (MFT-R4000, Lanzhou Institute of Chemical Physics, Chinese Academy of Sciences, Lanzhou, China) with a three-electrode system in $0.5 \, \text{mol/L} \, H_2 \text{SO}_4$ solutions. High-purity graphite was used as the counter electrode, the Fe–Al–Ti coatings acted as the working electrode, and a saturated calomel electrode was the reference electrode, as shown in Fig. 1. The load was applied by weights, and the sliding distance was adjusted by modifying the eccentric distance between the connecting rod and the turntable. The $H_2 \text{SO}_4$ solution was added to the Teflon electrolytic cell using a dropper. For the tribocorrosion test, the Fe–Al–Ti coatings were slid against 6 mm diameter Si_3N_4 ceramic balls. The Si_3N_4 ceramics have high hardness, chemical stability, low electrical

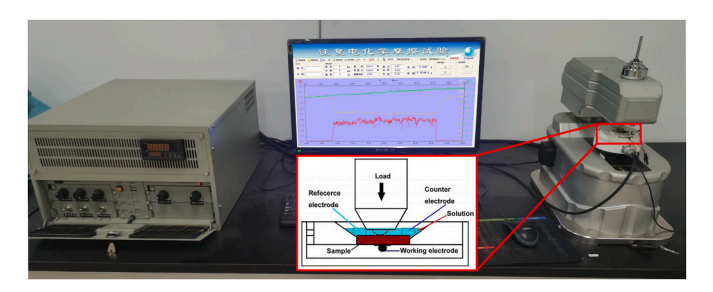


Fig. 1. Schematic diagram of tribocorrosion equipment.

conductivity, and excellent water lubrication effect and have demonstrated high potential for applications in aqueous environments [30]. The tribocorrosion tests were conducted at applied loads of 2 N, 5 N, 7 N, and 10 N, and induced Hertzian contact stresses were about 0.72 GPa, 0.94 Gpa, 1.24 GPa, and 1.63 GPa, respectively. The sliding frequency, run time, and sliding amplitude length was 2 Hz, 60 min, and 5 mm, respectively. A coating with an exposed area of 2.25 cm² was placed in a cell containing an H₂SO₄ solution. Prior to the tribocorrosion test, all specimens were immersed in an H₂SO₄ solution for 30 min to stabilize the OCP values. The OCP values were recorded for 30 min before tribocorrosion to stabilize the OCP. After the end of the sliding test, the OCP values were continuously recorded for 30 min to study the passivation characteristics of the Fe-Al-Ti coatings. The surface profiler (Alpha Step IQ) was then used to examine the area of each wear track depth profile for the Fe-Al-Ti coatings. The total wear volume was calculated by multiplying the cross-sectional area by the sliding distance. To facilitate comparison, the electrochemical corrosion resistance of the Fe-Al-Ti coatings was evaluated in 0.5 mol/L H_2SO_4 solutions under static corrosion and tribocorrosion conditions using a CHI660E electrochemical workstation. High-purity platinum was used as the counter electrode, the coatings were used as the working electrode (1 cm² exposure area) and a saturated calomel electrode (SCE) was used as the reference electrode. Prior to the electrochemical measurements, the samples were immersed in the 0.5 mol/L H₂SO₄ solution for 30 min to achieve a relatively stable potential. The potentials were swept from -0.6 V to +1.5 V (vs. SCE) at a sweep rate of 1 mV/s.

2.3. Coating characterization

Metallographic cross-sections of Fe-Al-Ti coatings were prepared using a standard mechanical polishing procedure and chemically etched in saturated FeCl3 and HCl solutions for 15-20 s. The microstructures of the coatings were examined by scanning electron microscopy (SEM, JSM-6700F, JEOL, Tokyo, Japan). The phase structures of the Fe-Al-Ti coatings were obtained by X-ray diffraction (XRD, D/Dmax-2400, Rigaku, Japan) with Cu K α radiation (λ =0.15418 nm). The scanning angle ranged from 20° to 90° at a scanning speed of 5°/min with a step size of 0.02°. The phase components were analyzed by energy-dispersive X-ray analysis (EDS, Link ISIS). The chemical states of the elements on tribocorrosion surfaces were determined by X-ray photoelectron spectroscopy (XPS) using a Kratos AXIS Ultra ESCA system with Al Ka (1486.6 eV) as the X-ray source. The accelerating voltage and emission current of the X-ray source were kept at 12 kV and 12 mA, respectively. The base pressure of the sample analysis chamber was maintained at $\sim 10^{-9}$ mbar, and the electron emission angle was 45°. Peak identification was performed by reference to an XPS database. Hardness profiles of the Fe-Al-Ti coatings were measured using a Vickers micro-hardness tester (HVS-1000, Yantai Huayin testing instrument Co., Ltd., China) with a load of 500 g and a load-dwell time of 15 s. All tests were repeated 3-5 times to ensure the reliability of the results.

3. Results and discussion

3.1. Microstructure

Fig. 2 shows the XRD patterns of the Fe–Al–Ti coatings prepared by the aluminothermic reaction. In Fig. 2 (a), the main phases of the Fe–25Al–5Ti coating are the B2 (Fe₃Al) and L2₁ (Fe₂TiAl). With increasing Ti content, the main phases of Fe–25Al–15Ti and Fe–25Al–25Ti coatings are L2₁ and C14 (Fe₂Ti) Laves phases. Additionally, all three coatings contained a small amount of Al₂O₃, which was mainly attributed to the incomplete removal of Al₂O₃ from the aluminothermic reaction products.

The typical microstructures of the Fe-Al-Ti coatings are shown in Fig. 3. It can be seen that the coatings have a uniform, compact microstructure with no obvious defects such as microcracks. The thickness of all coatings is about 1.2 mm-1.6 mm. The thickness of the coating is related to the total mass of the raw powders when the coating is relatively thin. The molten products are subject to overflow as the raw powder mass increases, which limits the further increase of the coating thickness. In Fig. 3(d-f), the coating shows a multi-phase structure, consisting of a white primary dendritic phase, a grey interdendritic phase, and a small amount of black phase. The chemical composition (at. %) of each phase was examined by EDS in Fig. 3(g-k). Based on the results of XRD and EDS analysis, it can be confirmed that the white phase is Fe₂TiAl, the grey interdendritic phase is Fe₂Ti or Fe₃Al and the black phase is Al₂O₃. With an increase in Ti content, the microstructures of Fe-Al-Ti coatings become more refined, which is beneficial for improving the strength and hardness of the coatings.

3.2. Microhardness

Fig. 4 shows the hardness distribution of the Fe–Al–Ti coatings and the indentation morphologies (Fe–25Al–25Ti coating) along the depth direction. The hardness of the coatings increases gradually with increasing Ti content. The average hardness of the Fe–25Al–25Ti coating is 565 HV, which is about three times higher than that of the 316L substrate (175 HV). It is worth noting that the middle area of the coatings is slightly softer than the top and bottom areas, which may be related to the lower cooling rate compared to the top and bottom areas. Typically, low cooling rates result in large grain sizes, which slightly soften the middle regions according to the Hall-Patch relationship [31]. Additionally, a small amount of high-hardness Al₂O₃ remains on the

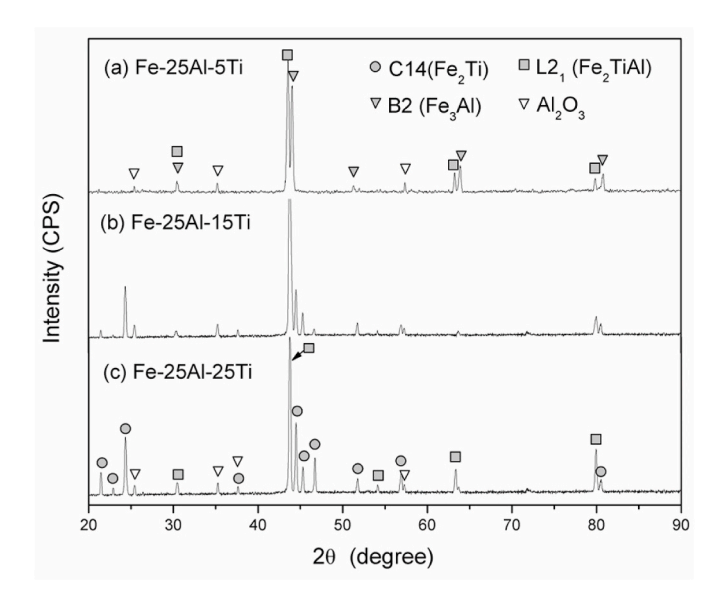


Fig. 2. X-ray diffraction patterns of the Fe–Al–Ti coatings prepared by the aluminothermic reaction.

surface of the coating, so the top region has a higher hardness.

3.3. Tribocorrosion behavior of the Fe-Al-Ti coatings

3.3.1. Effect of sliding wear on the electrochemical behavior

Fig. 5 shows the continuous variation of OCP for the 316L substrate and Fe-Al-Ti coatings sliding against Si₃N₄ balls before, during, and after the tribocorrosion tests. As shown in Fig. 5, the variation of OCP values for the 316L substrate and Fe-Al-Ti coatings during soaking was negligible. This indicated that a stable electrochemical state was formed on the surface of the samples. When the slide starts, the OCP value of the 316L substrate shows a steeply decreased and then a large fluctuation state. It is well known that the change in OCP is closely related to the electrochemical state of the materials [32]. Therefore, the apparent drop in OCP value can be attributed to the mechanical breakdown of the passivation film and the subsequent exposure to fresh metal surfaces with high electrochemical activity [33]. Compared to the 316L substrate, the OCP values of Fe-Al-Ti coatings decreased slightly and were more stable, which was attributed to the dynamic balance between the old passive film rupture and the new passive film establishment. The average OCP values of 316L substrate, Fe-25Al-5Ti, Fe-25Al-15Ti, and Fe-25Al-25Ti coatings during the tribocorrosion test were -0.37 V (vs. SCE), -0.18 V (vs. SCE), -0.12 V (vs. SCE), and -0.08 V (vs. SCE), respectively. Obviously, Fe-Al-Ti coatings have more positive OCP values, and the OCP values of the coatings increased with the increase in Ti content. This indicated that the high Ti content contributes to the coating's electrochemical corrosion resistance under tribocorrosion conditions. Once the sliding stopped, the OCP values for all samples gradually increased again, indicating that a new passivation film had been reconstructed on the worn track.

On the other hand, the friction coefficients of the Fe–Al–Ti coatings were more stable than that of the 316L substrate, and the friction coefficients of the coatings decreased during the tribocorrosion tests with the increase of Ti content, as shown in Fig. 5. The average friction coefficients of the 316L substrate, Fe–25Al–5Ti, Fe–25Al–15Ti, and Fe–25Al–25Ti coatings were 0.17, 0.14, 0.11 and 0.08, respectively. Thus, the high Ti content helps to reduce the friction coefficient of the coating/Si₃N₄ tribopairs. In summary, Fe–25Al–25Ti coatings with high Ti content exhibited higher hardness and good tribocorrosion performance compared to the other coatings. Therefore, to facilitate a comprehensive analysis of the tribocorrosion mechanism, the Fe–25Al–25Ti coating and 316L substrate were selected to evaluate the effects of electrochemical corrosion and friction loads on the tribocorrosion performance.

To investigate the effect of sliding contact on the corrosion behavior of 316L substrate and Fe-25Al-25Ti coating in 0.5 mol/L H₂SO₄ solutions, the potentiodynamic anodic polarization curves were performed to measure electrochemical parameters under corrosion-only and tribocorrosion conditions, as shown in Fig. 6. Meanwhile, the Tafel extrapolation method was used to obtain various electrochemical parameters from Fig. 6, and the results were listed in Table 1. During the pure corrosion process, Fe-25Al-25Ti coating shows better corrosion resistance with a higher corrosion potential (E_{corr}), wider passivation range, and higher breakdown potential (E_b) than the 316L substrate, as shown in Fig. 6 (a). The corrosion potential (E_{corr}), corrosion current density (i_{corr}), and breakdown potential (E_b) of Fe–25Al–25Ti coating are -0.13 V (vs. SCE), 1.64×10^{-6} A/cm², and 1.46 V (vs. SCE), respectively. Under the tribocorrosion condition, the polarization curves of the 316L substrate showed an obviously different, and the E_{corr} and i_{corr} of the 316L substrate were -0.45 V (vs. SCE) and 5.81 x 10^{-6} A/cm², respectively, which presented a lower corrosion potential and a higher anodic current density than that under corrosion-only condition, as shown in Fig. 6 (b) and Table 1. This indicated that wear behavior could accelerate corrosion during tribocorrosion. Meanwhile, severe fluctuations in current density were observed on the anodic polarization curve of the 316L substrate, which was attributed to the alternating effects of

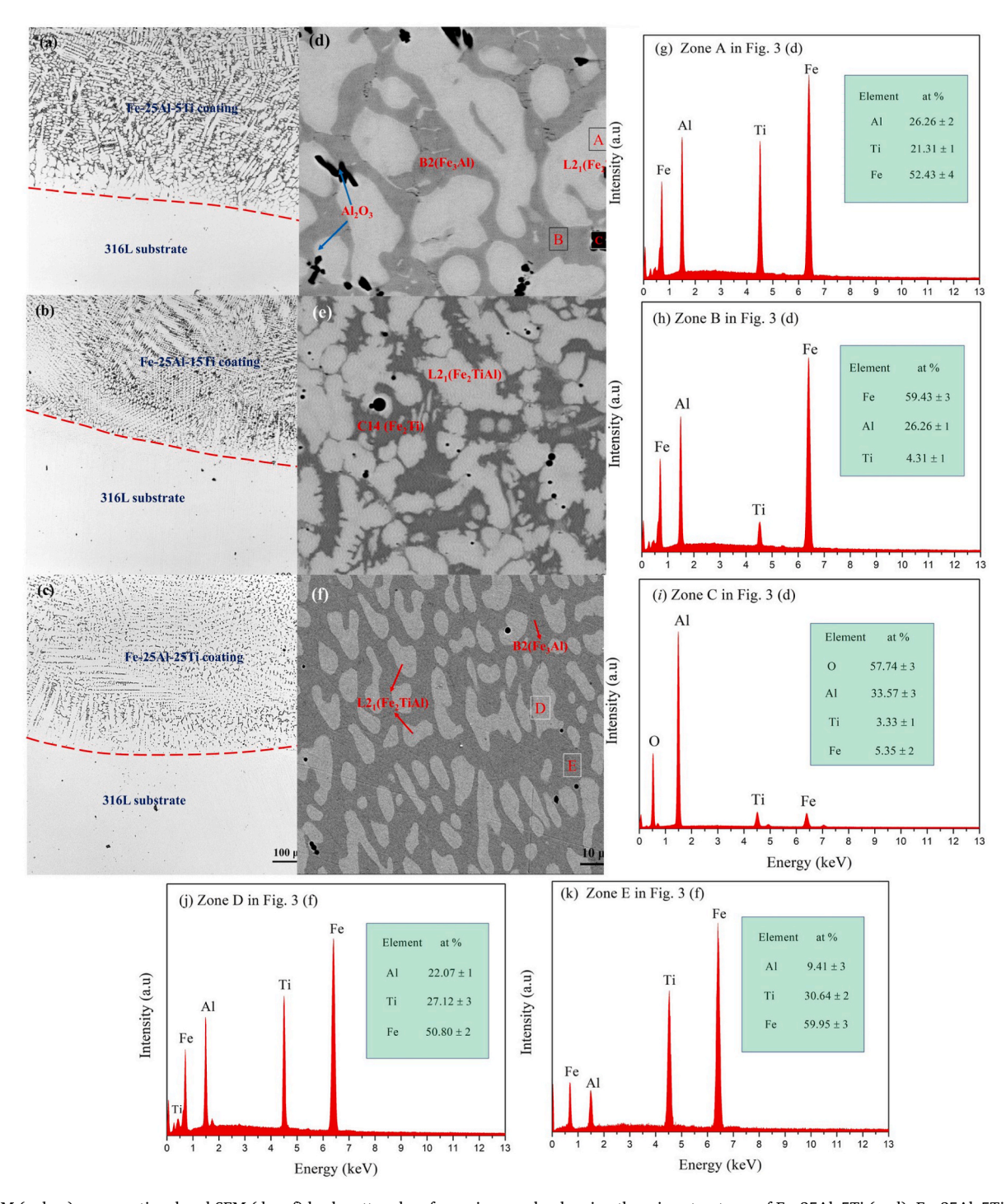


Fig. 3. OM (a, b, c) cross-sectional and SEM (d, e, f) backscattered surface micrographs showing the microstructures of Fe-25Al-5Ti (a, d), Fe-25Al-5Ti (b, e) and Fe-25Al-25Ti (c, f) coatings. (g-k) EDS results of Fe-Al-Ti coatings in Fig. 3 (d and f).

passivation film destruction and passivation during the tribocorrosion process. However, for the Fe–25Al–25Ti coating, the polarization curve was not significantly different, the E_{corr} and i_{corr} were slightly changed between corrosion-only and tribocorrosion. This indicates that the Fe–25Al–25Ti coating has a more stable characteristic during the tribocorrosion test in 0.5 mol/L H_2SO_4 solutions.

3.3.2. Friction and wear behavior under varying loads

The typical evolution of the friction coefficient of the 316L substrate and Fe–25Al–25Ti coating in 0.5 mol/L $\rm H_2SO_4$ solutions under different loads were shown in Fig. 7. The friction coefficient of the 316L substrate

and Fe–25Al–25Ti coating first increases rapidly (run-in period) and then tends to stabilize. The friction coefficient of the 316L substrate gradually increased with increasing the applied load, but the friction coefficient of the Fe–25Al–25Ti coating gradually decreased with increasing the load. Moreover, the friction coefficients of the Fe–25Al–25Ti coating under different loads were lower and more stable than those of the 316L substrate, indicating that the Fe–25Al–25Ti coating had a better lubrication effect in the $\rm H_2SO_4$ solution.

Fig. 8 shows the wear track of the 316L substrate and Fe–25Al–25Ti coating at different applied loads. In Fig. 8(a–c), the wear surface of the 316L substrate exhibited furrows and wear debris under all applied

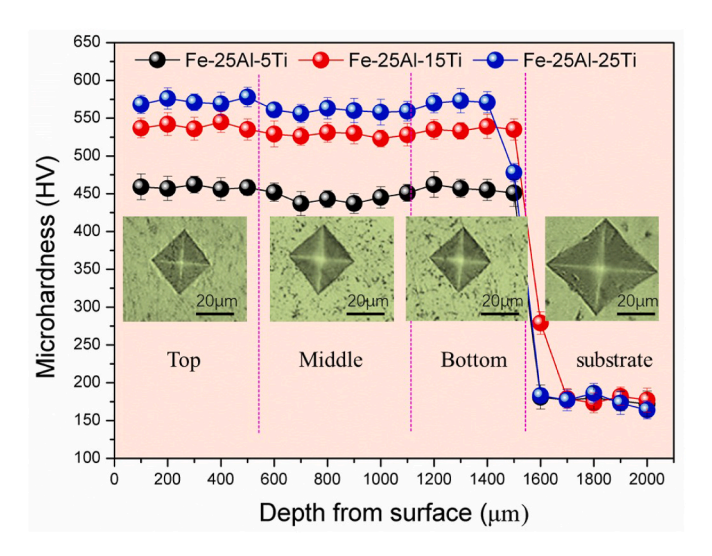


Fig. 4. Hardness distribution along the depth direction of the Fe–Al–Ti coatings.

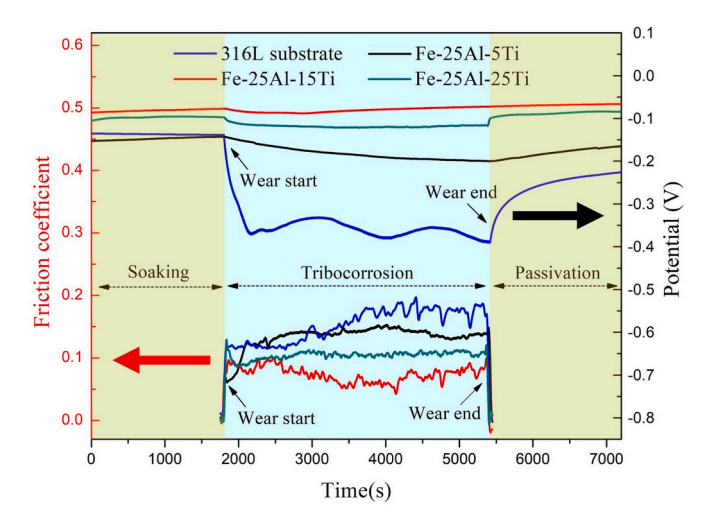


Fig. 5. OCP evolution and corresponding friction coefficient curves of 316L substrate and Fe–Al–Ti coating sliding against $\rm Si_3N_4$ balls in 0.5 mol/L $\rm H_2SO_4$ solutions.

loads, indicating that abrasive wear and plastic deformation were the primary wear mechanisms, which is consistent with the reports of Wang et al. [34]. In addition, a large number of corrosion products (black areas) were found in the wear track area, implying that corrosion plays

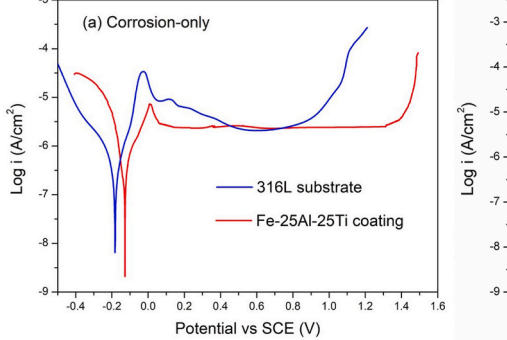
an important factor during the tribocorrosion test. At 10 N load, the wear scar width of 316L substrate was twice larger than that at 2 N load. For the Fe-25Al-25Ti coating, as shown in Fig. 8(d-f), the wear tracks were narrow and smooth, and no apparent defects were observed compared to the 316L substrate, indicating that the Fe-25Al-25Ti coating possesses excellent tribocorrosion resistance. Unlike the outer part of the wear scar, a typical microstructure composed of primary and interdendritic phases was found at the wear scar, similar to the metallographic corrosion, as shown in Fig. 8 (e and f). This difference can be attributed to wear-accelerated corrosion. In the local magnification of Fig. 8 (f), a selective tribocorrosion phenomenon was observed, and the tribocorrosion occurred mainly in the interdendritic phase (Fe₂Ti). The EDS analysis results in Fig. 8 (g and h) revealed that the tribocorrosion products on the coating surface contained Fe, Ti, Al, and O elements, and the presence of O elements indicated that the tribochemical reaction occurred during the tribocorrosion.

All other test conditions are the same, the friction coefficient is mainly controlled by the surface state of the material (such as roughness and lubrication characteristics). According to Fig. 8, for the 316L substrate, surface corrosion and wear became more severe with increasing load due to its low hardness and corrosion resistance, which deteriorated the surface characteristics of the tribological contact by generating more wear and corrosion products and increasing the surface roughness of 316L. Therefore, the friction coefficient of the 316L substrate gradually increased with increasing load. In contrast, the Fe–25Al–25Ti coating has high hardness and excellent corrosion resistance, so its friction coefficient is mainly affected by surface lubrication rather than roughness. With increasing load, the anodic corrosion products and the wear debris increase due to the interaction of wear and corrosion, which are good water lubricants [35], so the friction coefficients of the Fe–25Al–25Ti coating gradually decreased with increasing load.

On the other hand, the friction coefficient and corrosion resistance of materials are usually closely related to their surface composition and structural state [36]. The surface composition of the Fe–25Al–25Ti coating after the tribocorrosion test was examined by XPS analysis as

Table 1 Electrochemical parameters of 316L substrate and Fe–25Al–25Ti coating under the different conditions in 0.5 mol/L $\rm H_2SO_4$ solutions.

Condition	Samples	E _{corr} (V vs. SCE)	i_{corr} (10 ⁻⁶ A/cm ²)	E _b (V vs. SCE)
Corrosion- only	316L substrate	-0.19 ± 0.02	1.32 ± 0.02	0.84 ± 0.03
	Fe-25Al-25Ti	-0.13 ± 0.01	1.64 ± 0.03	1.46 ± 0.02
tribocorrosion	316L substrate	-0.45 ± 0.03	5.81 ± 0.03	0.56 ± 0.04
	Fe-25Al-25Ti	-0.16 ± 0.01	0.75 ± 0.02	$\begin{array}{c} \textbf{1.07} \; \pm \\ \textbf{0.01} \end{array}$



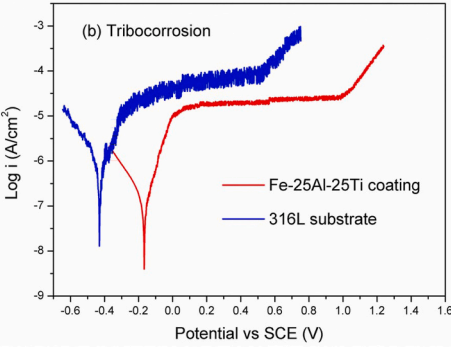


Fig. 6. Potentiodynamic polarization curves of 316L substrate and Fe–25Al–25Ti coating corrosion-only (a) and tribocorrosion conditions (b) in 0.5 mol/L H_2SO_4 solutions.

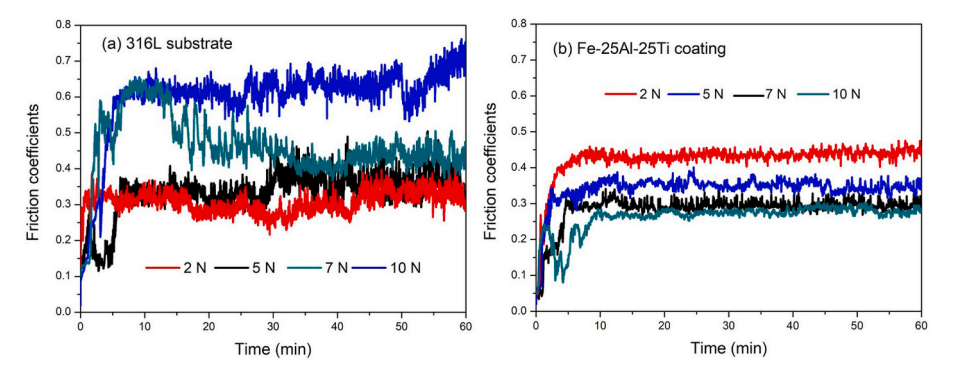


Fig. 7. Friction coefficients of the material sliding against the Si_3N_4 balls in 0.5 mol/L H_2SO_4 solutions under different loads: (a) 316L substrate, (b) Fe-25Al-25Ti coating.

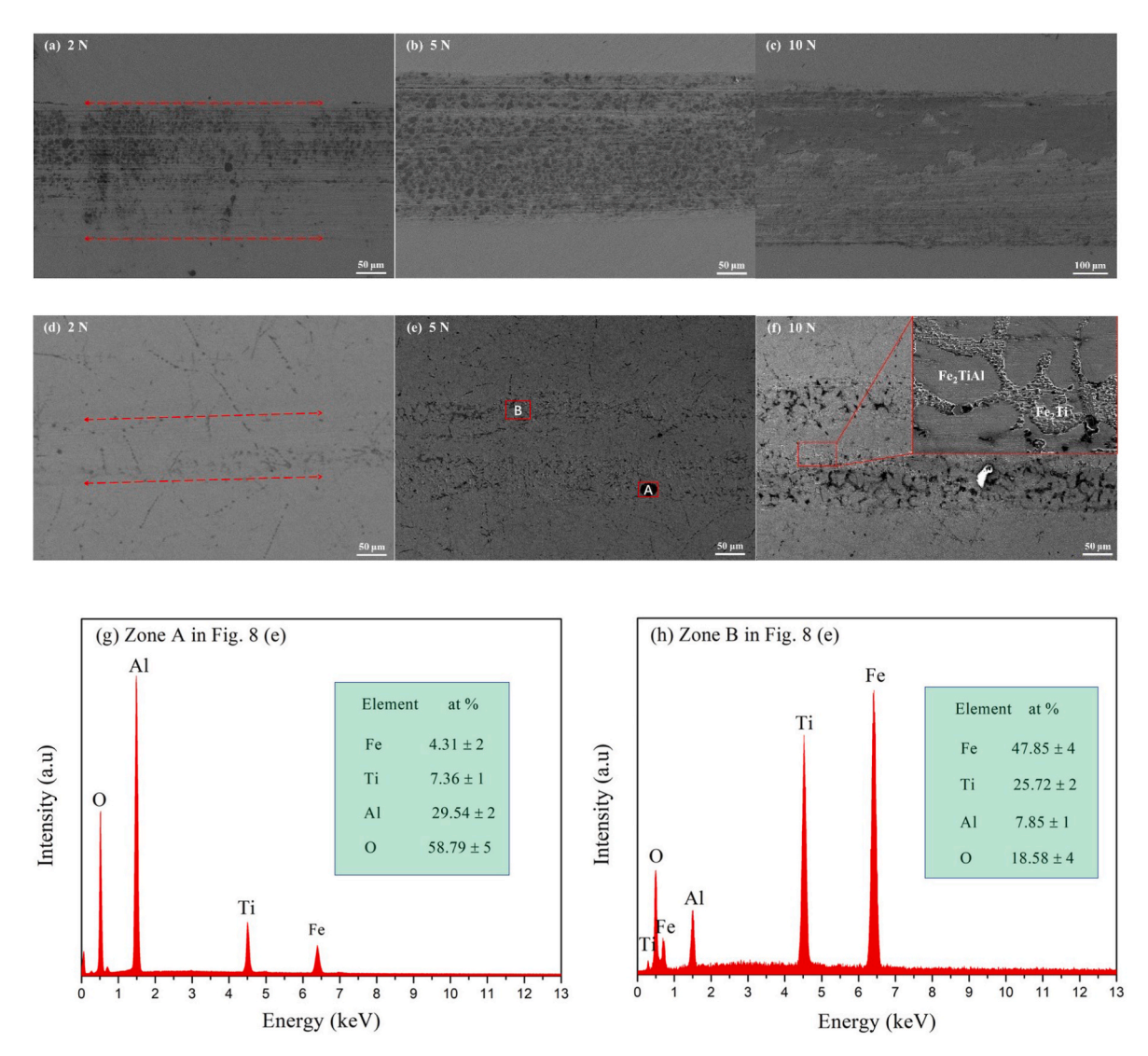


Fig. 8. SEM images of wear track for 316L substrate (a–c) and Fe–25Al–25Ti coating (d–f) under different applied loads; (g, h) EDS analysis of Zone A and Zone B in Fig. 8 (e).

shown in Fig. 9. In Fig. 9 (a), the broad scan spectrum shows peaks of Fe, Ti, Al, O, and C elements. Among them, the peaks of C 1s may originate from the contaminated hydrocarbon layer adsorbed on the coating surface. In Fig. 9 (b), the Ti 2p spectrum is composed of Ti $2p_{3/2}$ and Ti $2p_{1/2}$ double peaks at 458.68 eV and 463.98 eV, corresponding to the TiO₂ phase [37]. In Fig. 9 (c), a single Al 2p peak is located at a binding

energy of 74.3 eV, indicating that Al_2O_3 is formed on the surface of the Fe–25Al–25Ti coating [38]. The Fe 2p spectrum in Fig. 9 (d) indicates the presence of a small amount of Fe_2O_3 phase on the coating surface. The results of XPS analysis showed that a composite passivation layer composed of Al_2O_3 , TiO_2 , and Fe_2O_3 was formed on the surface of Fe–25Al–25Ti coating after tribocorrosion, which led to excellent

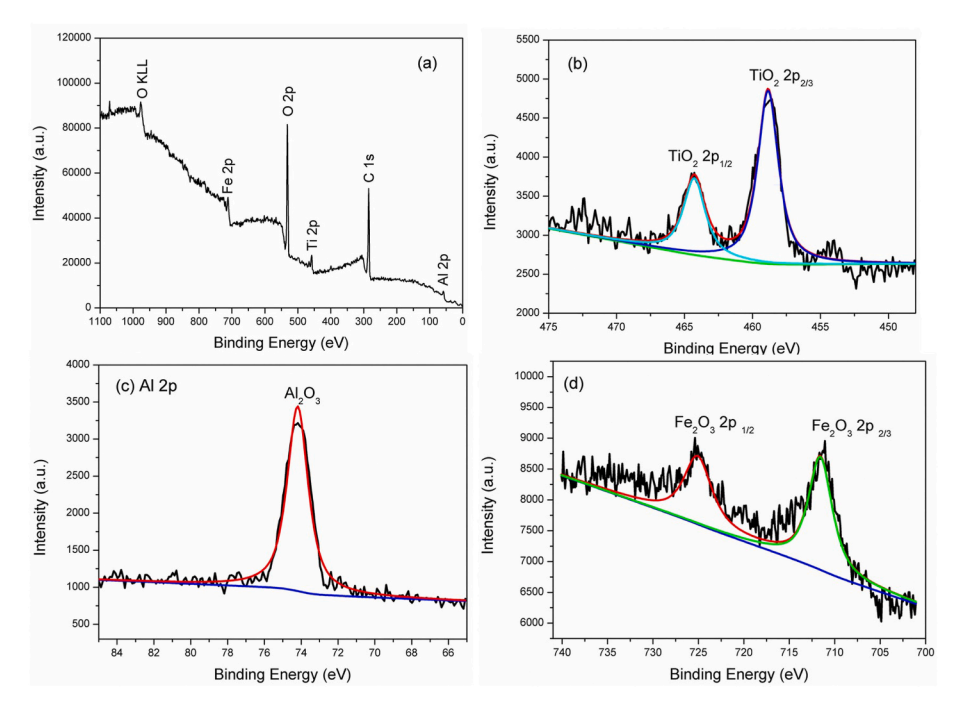


Fig. 9. XPS survey spectra (a) and high-resolution XPS spectra (b, c, and d) of Fe-25Al-25Ti coating after tribocorrosion test in 0.5 mol/L H₂SO₄ solutions.

corrosion resistance and low friction coefficient. In addition, the high hardness and good mechanical properties of the Fe–25Al–25Ti coating also contributed to its outstanding tribocorrosion properties.

To better understand the wear mechanism, the wear debris of Fe–25Al–25Ti coating after tribocorrosion in 0.5 mol/L $\rm H_2SO_4$ solutions was studied by the HRTEM technique. The TEM micrograph and corresponding EDS pattern (Fig. 10 (a)) showed that the wear debris was mainly composed of the Fe₂Ti phase, and an obvious microscopic plastic deformation was observed in the wear debris. Its HRTEM micrograph and corresponding FFT patterns were shown in Fig. 10 (b). The measured lattice spacings of the wear debris were 0.2389 nm, 0.3651 nm, and 0.2077 nm, which were consistent with the (110), (101) planes of C14–Fe₂Ti (PDF No. 65–0602) and the (220) plane of L2₁-Fe₂TiAl (PDF No. 54–0386), respectively.

For the 316L substrate and Fe–25Al–25Ti coating, which are both strongly passivated materials, corrosion and wear are mainly present in the tribocorrosion track area. However, some wear particles (third bodies) adhering to the wear track were observed (in Fig. 8), which adversely affected the measurement of the wear volume. According to N. Fillot's research [39] on the wear model and third body concept, wear should be considered as the loss of these third body particles for the whole wear track. In view of this, ultrasonic cleaning was performed on the wear surface of the 316L substrate and Fe–25Al–25Ti coating, and the surface morphology was shown in Fig. 11 (a) and (b). Compared to the original wear tracks (Fig. 8 (c and f)), a large number of adhering wear particles were removed from the cleaned wear tracks, while extensive grooves and selective tribocorrosion areas were observed after cleaning the surface. Fig. 11 (c and d) shows the SEM images of the wear

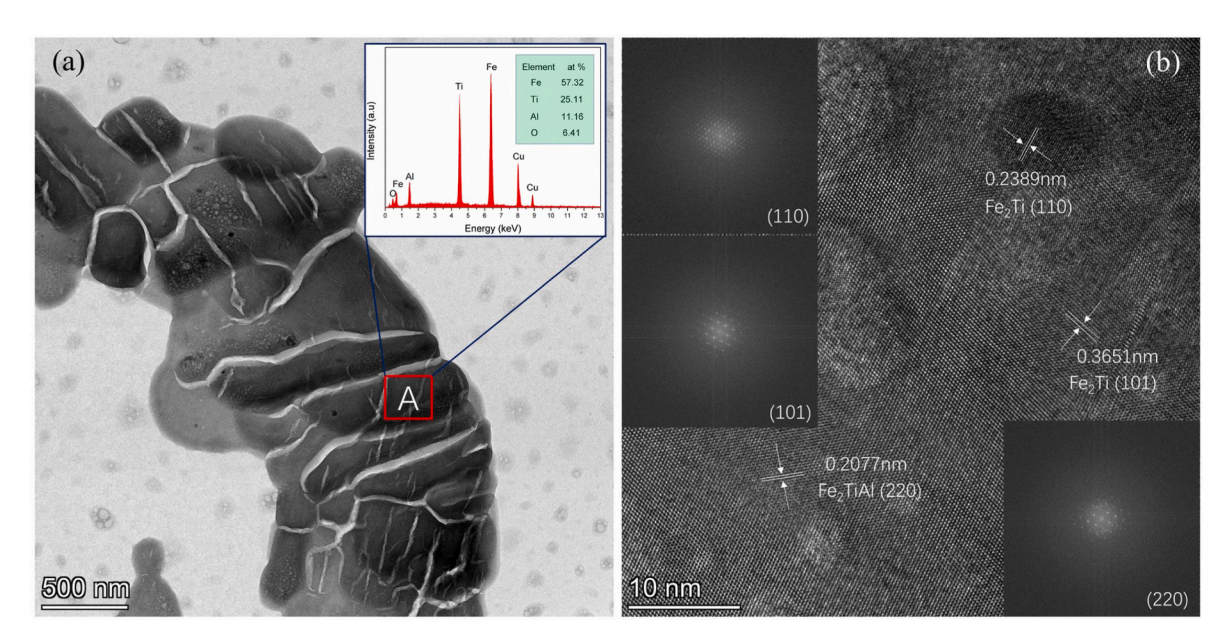
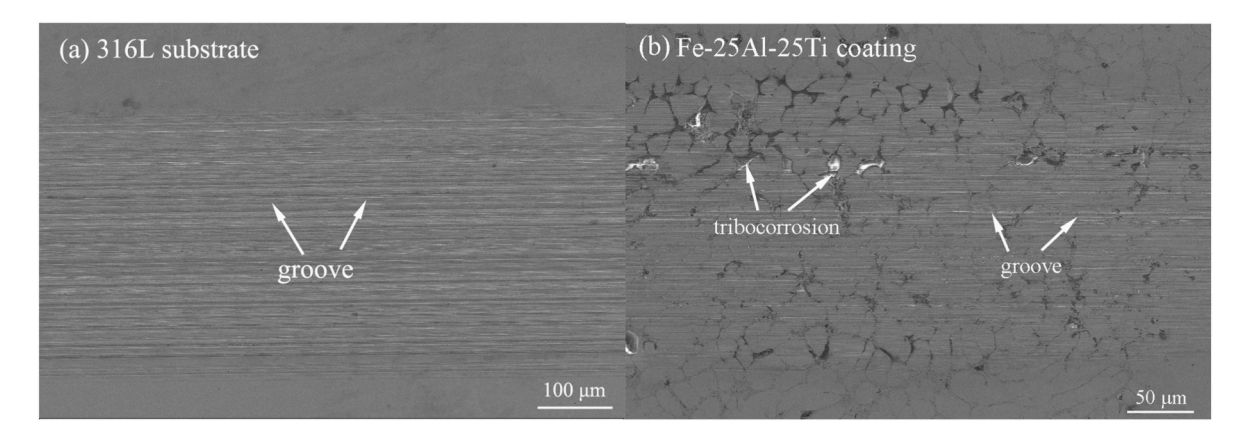
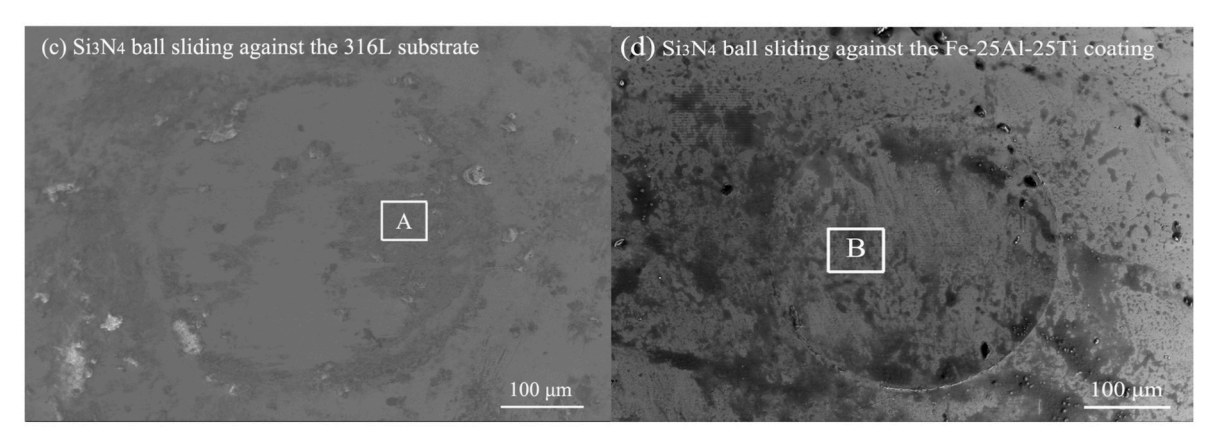


Fig. 10. TEM and HRTEM images of the wear debris of Fe-25Al-25Ti coating tribocorrosion test in 0.5 mol/L H $_2$ SO $_4$ solutions. (Insets: EDS and FFT patterns of the corresponding regions.)





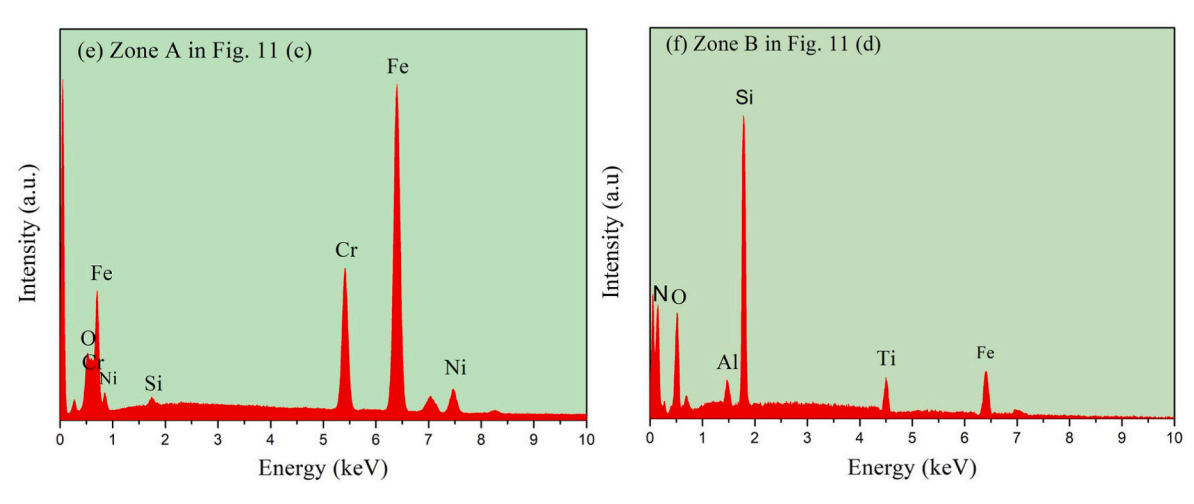
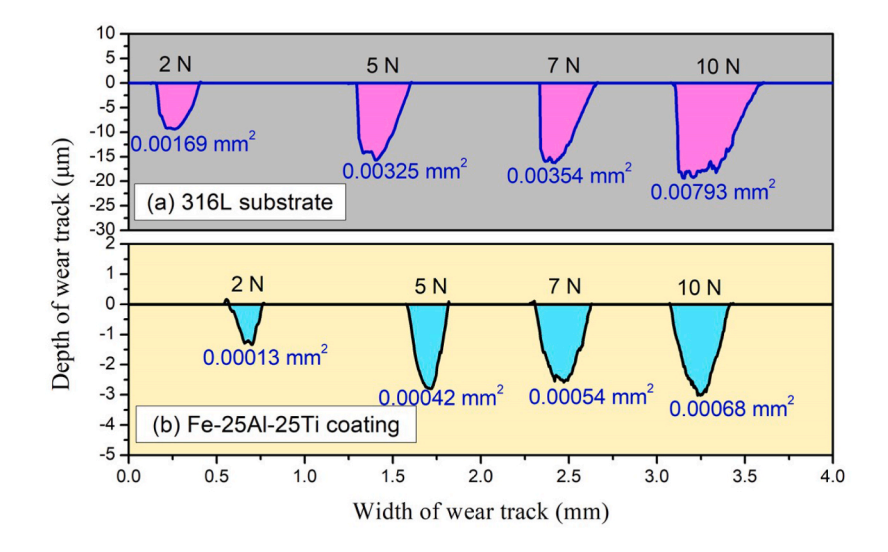


Fig. 11. SEM images and EDS spectra of the wear scars of the materials. (a, b) Cleaned wear scars of 316L substrate and Fe–25Al–25Ti coating under 10 N load, (c, d) Counter bodies (Si₃N₄ balls), (e, f) EDS analysis of regions A and B in Fig. 11 (c, d).

surfaces on Si_3N_4 balls after sliding against the 316L substrate and Fe–25Al–25Ti coating under the tribocorrosion condition. It can be observed that there is a clear contour on the wear surface of the counter bodies. The dimension of the Si_3N_4 ball wear scar area was larger after sliding against the 316L substrate compared to sliding against the Fe–25Al–25Ti coating. In Fig. 11 (c), some wear debris and tribocorrosion products were adhered to the surface and pushed to the edge of the wear scar. In contrast, the wear surface of the Si_3N_4 ball after sliding against the Fe–25Al–25Ti coating was smooth and clean, with no obvious wear debris adhering to the wear scar region, as shown in Fig. 11 (d). Combined with the results of EDS analysis of the worn surface of the Si_3N_4 balls after sliding against the 316L substrate (as shown

in Fig. 11(e)), the presence of Fe elements was observed, indicating that an apparent material transfer was generated from the 316L substrate to the counter body. However, this phenomenon can be ignored when sliding against the Fe–25Al–25Ti coating (in Fig. 11(f)).

Fig. 12 shows the cross-sectional profile and wear volume loss of the 316L substrate and Fe–25Al–25Ti coating at different applied loads. For the 316L substrate, the width, depth, and cross-sectional area of the wear track are significantly increased with increasing load. In contrast, the wear of Fe–25Al–25Ti coating is relatively mild under all applied loads, as shown in Fig. 12 (b). The corresponding wear loss variations for the 316L substrate and Fe–25Al–25Ti coating were shown in Fig. 12 (c). It was clear that the total material loss volume of the 316L substrate and



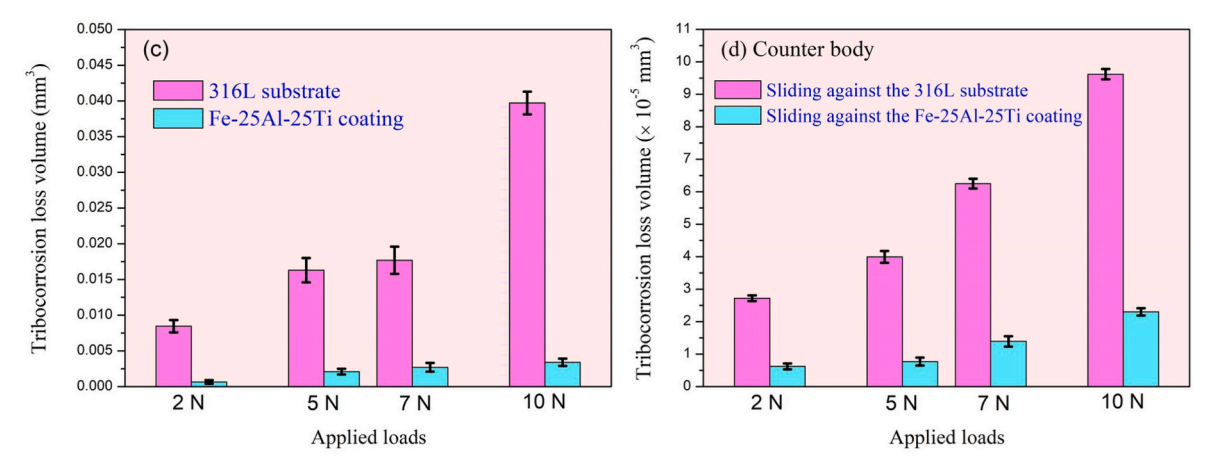


Fig. 12. Cross-sectional profiles (a, b) of the wear track and total wear volume loss (c, d) of the materials as a function of applied load: (c) 316L substrate and Fe-25Al-25Ti coating, (d) counter body.

Fe-25Al-25Ti coating increased as the applied load increased. However, the wear loss of the 316L substrate increases more rapidly with increasing applied load compared to the Fe-25Al-25Ti coating. The wear loss of the 316L substrate was up to 0.0397 mm³ when the applied load was 10 N, which was one order of magnitude higher than that of the Fe-25Al-25Ti coating. The Fe-25Al-25Ti coating exhibited lower wear loss under all applied loads due to its high hardness and excellent corrosion resistance. Fig. 12 (d) illustrates the wear loss of the counter body (Si₃N₄ balls) after sliding against the 316L substrate and Fe-25Al-25Ti coating. The results showed that the wear loss of the counter body gradually increased with the applied load. Moreover, the wear loss of the Si_3N_4 balls after sliding against the Fe-25Al-25Ti coating was significantly lower than that of the sliding against the 316Lsubstrate. This is close to the results obtained by Jia and Ma [40], who reported that the wear rates of Si₃N₄ balls against Fe₃Si-based alloys were significantly lower than those against AISI 304 stainless steel in water lubrication. The wear rate of Si₃N₄ was determined by a combination of mechanical wear (shearing, smearing, and microploughing) and tribochemical reactions with water $(Si_3N_4 + 12H_2O = 3Si(OH)_4 +$ 4NH₃) [41,42]. For a 316L substrate, wide wear marks represent large wear contact areas, while rough wear surfaces reduce the water-lubricating effect of Si₃N₄, resulting in high friction coefficients and wear rates for 316L/Si₃N₄ pairs. That is to say, Fe-25Al-25Ti coating was more suitable as a tribocorrosion-resistant material than 316L stainless steel.

3.3.3. Synergy between wear and corrosion

In practical applications, the interaction of wear and corrosion has a significant impact on material failure during the tribocorrosion process. Therefore, many efforts have been made by materials researchers to study the synergistic effects between wear and corrosion [7,43]. The material loss caused by the synergistic effect could be calculated by the general method proposed by Watson et al. [44]:

$$V_T = V_w + V_c + V_{wc} + V_{cw} (4)$$

Among them, V_T is the total material tribocorrosion loss volume, V_w is pure wear, V_c is corrosion-only, V_{wc} is wear-induced corrosion, and V_{cw} is corrosion-induced wear. Total material loss volume (V_T) and pure wear (V_w) were calculated based on the cross-sectional area of the wear track by a surface profilometer. In some studies, V_c and V_{wc} were calculated according to Faraday's law [45]:

$$V_c + V_{wc} = \frac{ItM}{nF\rho} \tag{5}$$

where I is the average current density, M is the relative atomic mass, t is the testing time, n is the valence variation, ρ is the material density and F is the Faraday constant. However, for multi-component materials (alloys or composites), the values of M, n, and ρ are difficult to calculate accurately, which makes the calculation results of material loss somewhat erroneous. The high-resolution ICP-OES (Inductively Coupled Plasma Optical Emission Spectrometer) technique has been widely used

for composition analysis and chemical corrosion due to its high detection sensitivity [46]. The solutions were extracted after tribocorrosion tests for analysis of metal content by the ICP-OES method and the results are shown in Fig. 13. According to Fig. 13, the values of V_c and V_{wc} were calculated using formula $V=m/\rho$, where *m* is the metal content in the solution, and ρ is the material density. The value of V_c was obtained from Fig. 6 (a) using the Tafel extrapolation method. In Fig. 13 (a), compared to the Al content, the content of Fe and Ti in the tribocorrosion solution of Fe-25Al-25Ti coating increased obviously with the increase of load, which further confirmed that the selective tribocorrosion of the interdendritic phase (Fe₂Ti) occurred during the tribocorrosion process. Compared to the Fe-25Al-25Ti coating, the metal content in the 316L substrate tribocorrosion solution was increased by an order of magnitude. Moreover, the metal content in the 316L substrate tribocorrosion solution increased more rapidly with increasing loads, as shown in Fig. 13 (b). V_{cw} cannot be measured directly, but it can be calculated using the following formula:

$$V_{cw} = V_T - V_c - V_{wc} - V_w (6)$$

Fig. 14 shows the evolution of each partial contribution of the 316L substrate and Fe–25Al–25Ti coating to the total wear volume loss with the increasing load. As seen in Fig. 14, the corrosion-only (V_c) and wear-induced corrosion (V_{wc}) of Fe–25Al–25Ti coatings account for a small percentage of material loss, all less than 6%. The percentage of the synergistic effect (V_{cm} and V_{mc}) of the 316L substrate and Fe–25Al–25Ti coating increased and the V_m decreased with increasing applied load. The material loss was dominated by the synergistic effects of wear and corrosion. For the 316L substrate, the main volume loss is changed from V_m to V_{cm} with increasing applied load from 2 N to 10 N, indicating that corrosion-induced wear gradually occupied a dominant position. For the Fe–25Al–25Ti coating, the main volume loss is still attributed to the pure mechanical wear of V_m .

3.3.4. Tribocorrosion mechanism

In fact, the tribocorrosion properties of materials mainly depend on their microstructure, mechanical properties, and corrosion resistance. For the 316L substrate, once the passivation film was discontinuous or broken, the exfoliated hard particles rolled or moved along the sliding direction to form a three-body, and accelerated the wear of the 316L substrate. Moreover, when the passivation film on the surface was removed, the fresh surface was exposed to an H₂SO₄ solution, so microscopic galvanic corrosion could occur between the wear track and the passivation area. In addition, the high anodic current density of the 316L substrate (Fig. 6 (b)) implied a high corrosion rate in the tribocorrosion test. This was consistent with the high material loss of corrosion-induced wear (V_{cw} = 48.59%) for the 316L substrate. In contrast, the high exothermic and rapid cooling of the aluminothermic casting process conferred high hardness, compactness, and compositional uniformity to the Fe-25Al-25Ti coating, which effectively improved its wear and corrosion resistance. As seen in Fig. 8, the wear

track of the Fe-25Al-25Ti coating was shallower and narrower than that of the 316L substrate, the narrow wear track represents less fresh surface area exposure to solution and weaker galvanic corrosion. With increasing load, the Fe-25Al-25Ti coating will undergo selective tribocorrosion of the Fe₂Ti phase as shown in the high-magnification photograph in Fig. 8 (f). Firstly, the Fe₂TiAl ternary phase has a better combination of strength, hardness and toughness compared to the Fe₂Ti phase [19,47], and the hardness and fracture toughness of Fe₂TiAl and Fe₂Ti are (532 \pm 35 HV and 8.9 MPa m $^{-1/2}$) and (584 \pm 28 HV and 1 $\overline{\text{MPa}}\ \text{m}^{-1/2}$), respectively. Usually, the wear rate is inversely proportional to the hardness and fracture toughness of the material under adhesive and abrasive wear conditions according to the wear equation $(W \propto K_{IC}^{-3/4} H^{-1/2})$, where K_{IC} is the fracture toughness and H is the hardness of the material) [48]. This enables Fe₂TiAl to have a better wear resistance than that of Fe₂Ti. Secondly, the Ti and Al elements in Fe₂TiAl are susceptible to passivation, and especially the synergistic effect of Ti and Al can further improve the corrosion resistance of the alloy in acidic and neutral media [49,50]. Therefore, Fe₂TiAl has better tribocorrosion resistance than the Fe₂Ti phase. This also explained that the content of Fe and Ti in the tribocorrosion solution of the Fe-25Al-25Ti coating increased significantly with the increase of load (in Fig. 13 (a)). Moreover, the tribolayer composed of Al₂O₃, TiO₂, and Fe₂O₃ has good lubrication and corrosion obstacles, which reduces the tribocorrosion rate of the coating. Even if the protective layers of Al₂O₃, TiO2, and Fe2O3 were broken, the Fe-25Al-25Ti coating could still prevent mechanical wear and intrusion of sulfuric acid solution due to the phase composition of Fe₂TiAl and Fe₂Ti intermetallic compounds with high hardness, excellent chemical stability and strong covalent-dominant atomic bonds.

4. Conclusions

In the present work, Fe–Al–Ti coatings with different Ti contents were successfully prepared on 316L substrates by the SHS process using an aluminothermic reaction. The tribocorrosion behaviors of the 316L substrate and Fe–Al–Ti coatings were investigated in 0.5 mol/L $\rm H_2SO_4$ solutions. The conclusions are summarized as follows:

- (1) The Fe–Al–Ti coatings have a multi-phase microstructure composed of Fe $_3$ Al, Fe $_2$ TiAl, Fe $_2$ Ti and a small amount of Al $_2$ O $_3$, and are metallurgically bonded to the substrate. Compared with the 316L substrate, the hardness of the Fe–Al–Ti coating is significantly improved.
- (2) When the sliding started, the OCP values of Fe–Al–Ti coatings decreased significantly during the tribocorrosion test, indicating a strong wear-corrosion synergistic effect. Compared to 316L substrate, Fe–25Al–25Ti coating is more suitable as a tribocorrosion protective material in 0.5 mol/L H₂SO₄ solutions with a high OCP value, low friction coefficient and wear loss due to the

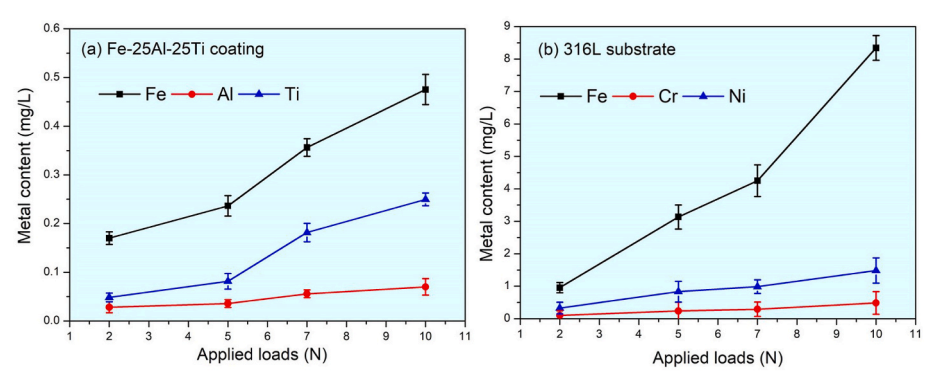


Fig. 13. Evolution of the metal contents under different loads after the tribocorrosion tests for 60 min. (a) Fe-25Al-25Ti coating, (b) 316L substrate.

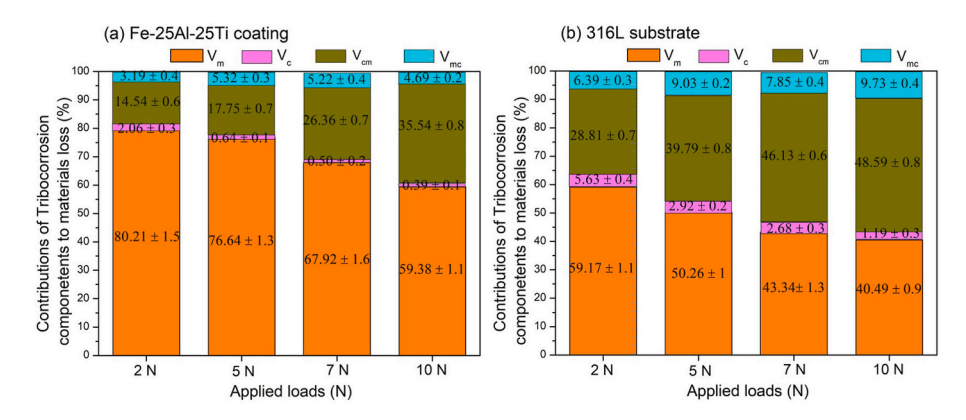


Fig. 14. Contributions of tribocorrosion components under different applied loads in H₂SO₄ solution: (a) Fe-25Al-25Ti coating, (b) 316L substrate.

formation of stable, compact, and well-lubricated Al_2O_3 , TiO_2 , and Fe_2O_3 protective film on the surface.

(3) The wear volume loss of the 316L substrate is about one order of magnitude higher than that of the Fe–25Al–25Ti coating. Selective tribocorrosion of the interdendritic phase (Fe₂Ti) occurred during tribocorrosion. The percentage of synergistic effect (V_{cm} and V_{mc}) of the 316L substrate and Fe–25Al–25Ti coating was increased and the V_m was decreased with increasing applied load.

CRediT authorship contribution statement

- **H. Chen:** Formal analysis, Investigation, Writing an original draft, Writing a review, and editing.
 - R.P. Li: Acquisition of data, Investigation, Writing an original draft.
 - S. Guo: Formal analysis, Writing review, and editing.
 - Z. Zhang: Investigation, Writing an original draft.
 - X.X. Li: Acquisition of data.
 - X.L. Zhao: Investigation, Acquisition of data.

Declaration of competing interest

The authors declare that they have no known competing financial interests or personal relationships that could have appeared to influence the work reported in this paper.

Data availability

Data will be made available on request.

Acknowledgments

This research was supported by the Natural Science Foundation of Shandong Province of China (Grant Nos. ZR2021ME204, ZR2020QE004, and ZR2020QE028). The authors acknowledge Mr. Deshun Liu for their assistance in the experiments of annealing.

References

- [1] L.X. Dong, H.M. Wang, Microstructure and corrosion properties of laser-melted deposited Ti₂Ni₃Si/NiTi intermetallic alloy, J. Alloys Compd. 465 (2008) 83–89.
- [2] L. Yuan, H.M. Wang, Corrosion behaviors of a γ-toughened Cr₁₃Ni₅Si₂/Cr₃Ni₅Si₂ multi-phase ternary metal silicide alloy in NaCl solution, Electrochim. Acta 54 (2008) 421–429.
- [3] H. Chen, Z. Zhang, X.H. Hao, B.X. Huang, X.C. Zhao, C.C. Hu, Microstructure and tribocorrosion properties of NiTi/AlNi₂Ti ternary intermetallic alloy, Vacuum 184 (2021), 109928.
- [4] M. Mehdipour, R. Naderi, B.P. Markhali, Electrochemical study of effect of the concentration of azole derivatives on corrosion behavior of stainless steel in H₂SO₄, Prog. Org. Coating 77 (2014) 1761–1767.
- [5] L.Y. Li, J. Yan, J. Xiao, L. Sun, H.Y. Fan, J. Wang, A comparative study of corrosion behavior of S-phase with AISI 304 austenitic stainless steel in H₂S/CO₂/Cl- media, Corrosion Sci. 187 (2021), 109472.

- [6] R.T. Loto, Effect of elevated temperature variations on the corrosion resistance of S31603 and SS2562 austenitic stainless steels in chloride-sulphate environments, J. Mater. Res. Technol. 8 (2019) 5415–5421.
- [7] Q. Chen, Y.Z. Gao, Z.W. Xie, T. Chen, Y.Y. Wan, H. Wang, X. Gao, Y. Chen, Y. W. Zhou, Y.Y. Guo, Tribocorrosion behaviors of CrN coating in 3.5 wt% NaCl solution. Thin Solid Films 622 (2017) 41–47.
- [8] H.M. Wang, G. Duan, Wear and corrosion behavior of laser clad Cr₃Si reinforced intermetallic composite coatings, Intermetallics 11 (2003) 755–762.
- [9] H.M. Wang, C.M. Wang, L.X. Cai, Wear and corrosion resistance of laser clad Ni₂Si/ NiSi composite coatings, Surf. Coat. Technol. 168 (2003) 202–208.
- [10] Q. He, C.C. Jia, J. Meng, Mechanical properties and microstructure of Fe₃Al intermetallics fabricated by mechanical alloying and spark plasma sintering, T. Nonferr. Metal Soc. 16 (2006) 1995–1999.
- [11] N. Park, S.C. Lee, P.R. Cha, Effects of alloying elements on the stability and mechanical properties of Fe₃Al from first-principles calculations, Comput. Mater. Sci. 146 (2018) 303–309.
- [12] M.Y. Niu, X.H. Zhang, J. Yang, Tribological behaviour of Fe₃Al-Ba_{0.25}Sr_{0.75}SO₄ self-lubricating composites in vacuum and air, Vacuum 154 (2018) 315–321.
- [13] S. Takesue, Y. Misaka, J. Komotori, Formation of Fe-Al intermetallic compound layer by AIH-FPP and its effect on tribological properties of stainless steel, ISIJ Int. 61 (2021) 1946–1954.
- [14] H.D. Wang, Q.Q. Wang, H. Liu, P.Q. La, Z.N. Li, Effect of Cr content on microstructure and mechanical properties of annealed large-dimensional bulk nanocrystalline Fe-Al-Cr alloys by self-propagating combustion synthesis, Mater. Express 9 (2019) 641–647.
- [15] C.D. Arrieta-Gonzalez, R.A. Rodriguez-Diaz, J. Mayen, R.F. Retes-Mantilla, M. T. Torres-Mancera, L.A. Oros-Mendez, H. Cruz-Mejia, N.S. Flores-Garcia, J. Porcayo-Calderon, Electrochemical performance of Fe40Al-X (X = Cr, Ti, Co, Ni) alloys exposed to artificial saliva, Materials 13 (2020) 1–20.
- [16] M. Kwiatkowska, D. Zasada, J. Bystrzycki, M. Polanski, Synthesis of Fe-Al-Ti based intermetallics with the use of laser engineered net shaping (LENS), Materials 8 (2015) 2311–2331.
- [17] M.L. Busurina, A.E. Sytschev, A.V. Karpov, N.V. Sachkova, I.D. Kovalev, Peculiarities of the structure and phase formation of the Fe₂TiAl Heusler alloy during self-propagating high temperature synthesis (SHS), Russ. J. Phys. Chem. B 14 (2020) 999–1006.
- [18] R. Krein, M. Palm, The influence of Cr and B additions on the mechanical properties and oxidation behavior of L2₁-ordered Fe–Al–Ti-based alloys at high temperatures, Acta Mater. 56 (2008) 2400–2405.
- [19] M. Palm, G. Sauthoff, Deformation behaviour and oxidation resistance of singlephase and two-phase L2₁-ordered Fe–Al–Ti alloys, Intermetallics 12 (2004) 1345–1359.
- [20] R. Krein, M. Friak, J. Neugebauer, M. Palm, M. Heilmaier, L2 $_1$ -ordered Fe–Al–Ti alloys, Intermetallics 18 (2010) 1360–1364.
- [21] R. Krein, M. Palm, M. Heilmaier, Characterisation of microstructures, mechanical properties, and oxidation behavior of coherent A2 + L2₁ Fe-Al-Ti alloys, J. Mater. Res. 24 (2009) 3412–3421.
- [22] X.K. Liu, C. Liu, Z. Zheng, X.H. Lan, First-principles investigation on the structural and elastic properties of cubic-Fe₂TiAl under high pressures, Chin. Phys. B 8 (2013) 561, 566.
- [23] A.J. Panas, C. Senderowski, B. Fikus, Thermophysical properties of multiphase Fe-Al intermetallic-oxide ceramic coatings deposited by gas detonation spraying, Thermochim, Acta 676 (2019) 164–171.
- [24] G.X. Hu, Z.X. Xu, J.J. Liu, Y.H. Li, Microstructure and corrosion resistance of simultaneous Al-Fe coating on copper by pack cementation, Surf. Coat. Technol. 203 (2009) 3392–3397.
- [25] A. Grigoriev, I. Polozov, V. Sufiiarov, A. Popovich, In-situ synthesis of Ti₂AlNb-based intermetallic alloy by selective laser melting, J. Alloys Compd. 704 (2017)
- [26] H. Sasaki, M. Maeda, Siliconizing of iron and molybdenum by electrochemical reduction of silicon in molten SiO₂-Li₂O-MgO, J. Alloys Compd. 641 (2015) 64–68.
- [27] R. Sitek, J. Kaminski, J. Borysiuk, H. Matysiak, K. Kubiak, K.J. Kurzydlowski, Microstructure and properties of titanium aluminides on Ti6Al4V titanium alloy produced by chemical vapor deposition method, Intermetallics 36 (2013) 36–44.

- [28] P.Q. La, X.J. Zhen, X.F. Lu, Y.P. Wei, C.L. Li, S.L. Hu, Effects of different substrates on microstructures and mechanical properties of a bimodal bulk nano/micro grained 1020 carbon steels prepared by aluminothermic reaction casting, Adv. Eng. Mater. 16 (2014) 211–217.
- [29] G. Wang, S.Q. Jiang, Z.H. Wang, D. Cai, Y. Yi, Z.H. Zhou, Self-propagating high-temperature synthesis of Al₂O₃-TiB₂ coatings by aluminothermic reactions, Rare Met. Mater. Eng. 41 (2012) 215–218.
- [30] M. Chen, K. Kato, K. Adachi, The comparisons of sliding speed and normal load effect on friction coefficients of self mated Si₃N₄ and SiC under water lubrication, Tribol. Int. 35 (2002) 129–135.
- [31] B. Yang, L. Huang, A. Qi, J. Shan, G. Lin, X. Ma, Wire-feed deposition TiB reinforced Ti composite coating: formation mechanism and tribological properties, Mater. Lett. 229 (2018) 221–224.
- [32] L. Shan, Y. Wang, Y. Zhang, Q. Zhang, Q. Xue, Tribocorrosion behaviors of PVD CrN coated stainless steel in seawater, Wear 362–363 (2016) 97–104.
- [33] F.L. Ma, J.L. Li, Z.X. Zeng, Y.M. Gao, Structural, mechanical and tribocorrosion behavior in artificial seawater of CrN/AlN nano-multilayer coatings on F690 steel substrates, Appl. Surf. Sci. 15 (2018) 404–414.
- [34] Y.W. Ye, Y.X. Wang, X.L. Ma, D.W. Zhang, L.P. Wang, X.G. Li, Tribocorrosion behaviors of multilayer PVD DLC coated 304L stainless steel in seawater, Diam. Relat. Mater. 79 (2017) 70–78.
- [35] Y.Q. Fu, F. Zhou, M.D. Zhang, Q.Z. Wang, Z.F. Zhou, Structural, mechanical and tribocorrosion performances of CrMoSiN coatings with various Mo contents in artificial seawater, Appl. Surf. Sci. 525 (2020), 146629.
- [36] Y.Q. Fu, F. Zhou, Q.Z. Wang, M.D. Zhang, Z.F. Zhou, Electrochemical and tribocorrosion performances of CrMoSiCN coating on Ti-6Al-4V titanium alloy in artificial seawater, Corrosion Sci. 165 (2020), 108385.
- [37] Q. Chen, Z.W. Xie, T. Chen, F. Gong, Tribocorrosion failure mechanism of TiN/SiOx duplex coating deposited on AISI304 stainless steel, Materials 9 (2016) 963–975.
- [38] J. Xu, L.L. Liu, P. Munroe, Z.H. Xie, Z.T. Liang, The nature and role of passive films in controlling the corrosion resistance of MoSi₂-based nanocomposite coatings, J. Mater. Chem. 1 (2013) 10281–10291.

- [39] N. Fillot, I. Iordanoff, Y. Berthoer, Wear modeling and the third body concept, Wear 262 (2007) 949–957.
- [40] J.G. Jia, Q. Ma, J.J. Lu, B. Wang, Reciprocating sliding friction and wear property of Fe₃Si based alloys containing Cu in water lubrication, Tribol. Lett. 30 (2008) 113-121
- [41] R.C. Dante, C.K. Kajdas, A review and a fundamental theory of silicon nitride tribochemistry, Wear 288 (2012) 27–38.
- [42] F. Zhou, X.L. Wang, K. Kato, Z.D. Dai, Friction and wear property of a-CNx coatings sliding against Si_3N_4 balls in water, Wear 263 (2007) 1253–1258.
- [43] A. Hatem, J.L. Lin, R.H. Wei, R. Torres, D.C. Laurindo, G.B.D. Souza, P. Soares, Tribocorrosion behavior of low friction TiSiCN nanocomposite coatings deposited on titanium alloy for biomedical applications, Surf. Coat. Technol. 347 (2018) 1, 12
- [44] S.W. Watson, F.J. Friedersdorf, B.W. Madsen, S.D. Cramer, Methods of measuring wear-corrosion synergism, Wear 181 (1995) 476–484.
- [45] L. Shan, Y.X. Wang, Y.R. Zhang, Q. Zhang, Q.J. Xue, Tribocorrosion behaviors of PVD CrN coated stainless steel in seawater, Wear 362–363 (2016) 97–104.
- [46] M.T. Mathewa, T. Utha, N.J. Hallaba, R. Pourzalb, A. Fischerb, M.A. Wimmera, Construction of a tribocorrosion test apparatus for the hip joint: validation, test methodology and analysis, Wear 271 (2011) 2651–2659.
- [47] U. Prakash, G. Sauthoff, Structure and properties of Fe-Al-Ti intermetallic alloys, Intermetallics 9 (2001) 107–112.
- [48] H.A. Zhang, X.P. Hu, J.H. Yan, P. Chen, S.W. Tang, Dry sliding wear behaviors of La₂O₃-WSi₂-MoSi₂ composite against alloy steel, Wear 260 (2006) 903–908.
- [49] Y. Qiu, S. Thomas, M.A. Gibson, H.L. Fraser, K. Pohl, N. Birbilis, Microstructure and corrosion properties of the low-density single-phase compositionally complex alloy AlTiVCr, Corrosion Sci. 133 (2018) 386–396.
- [50] G. Priyotomo, S. Wagle, K. Okitsu, A. Iwase, Y. Kaneno, R. Nishimura, T. Takasugi, The corrosion behavior of Ni₃(Si,Ti) intermetallic compounds with Al, Cr, and Mo in various acidic solutions, Corrosion Sci. 60 (2012) 10–17.